Measurements of Surface Deformation in Highly-Reflecting Liquid-Metals

Pablo Gutiérrez, Vincent Padilla and Sébastien Aumaître

Abstract We present an experimental study of surface deformation in a liquid metal. The investigation has two main parts. First we present an optical setup allowing to obtain the surface profile along a line, for a highly-reflecting liquid-metal. We track the diffusion of a laser sheet on the surface from two opposite angles, avoiding saturations due to specular reflection. In the second part, the technique is used to study some aspects of the wave-vortex interaction problem. Special attention is given to the surface deformation produced by a flow composed by moving vortices. Asymmetric height statistics are observed and discussed. Some indications of wave emission are presented. Finally, the attenuation of propagating waves by the same flow is briefly discussed.

1 Introduction

It is difficult to think about a world without waves. Waves are everywhere: sometimes they are visible to the eye and sometimes not. This chapter deals with waves in fluids. And even if these waves are visible to our eyes, they can be elusive to quantification. Such a challenge is usually overcome with a thorough use of light (which is, in fact, electromagnetic waves), as it will be discussed here from an experimental point of view.

P. Gutiérrez (✉)
Departamento de Física, Facultad de Ciencias Físicas y Matemáticas,
Universidad de Chile, Casilla 487-3, Santiago, Chile
e-mail: pagutier@gmail.com

P. Gutiérrez · V. Padilla · S. Aumaître
Service de Physique de l'Etat Condensé, DSM, CEA-Saclay, UMR-CNRS 3680,
91191 Gif-sur-Yvette, France

S. Aumaître
Laboratoire de Physique, ENS de Lyon, UMR-CNRS 5672, 46 allée d'Italie,
69007 Lyon, France

M. Tlidi and M.G. Clerc (eds.), *Nonlinear Dynamics: Materials, Theory and Experiments*, Springer Proceedings in Physics 173,
DOI 10.1007/978-3-319-24871-4_18

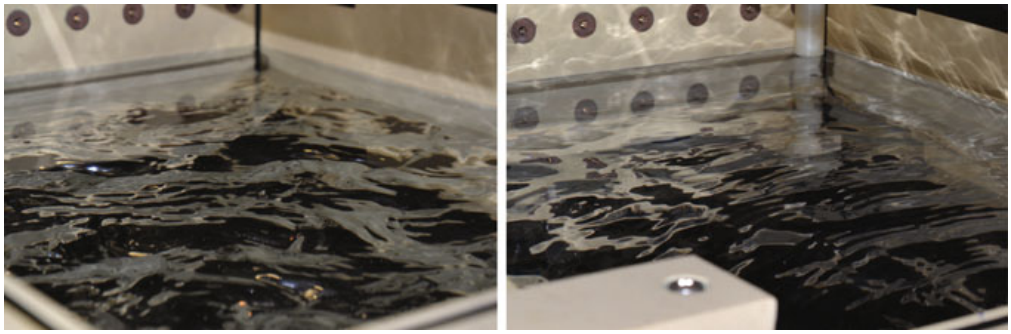

Fig. 1 Flows under consideration, exhibiting wave-like motion on the surface. A liquid metal is driven with the Lorentz force (see Sect. 3). *Left* highly fluctuating motion when the forcing is strong ($I = 400$ A). *Right* with a gentle forcing ($I = 80$ A), a linear wave is excited at 5 Hz from a corner of the container

More generally, we are interested in the motion of the free surface of a liquid. It happens both because of the influence of an underlying turbulent motion, or because of the external perturbation of the surface. Theoretical studies of the generation of waves from turbulent motion can be traced back to Lighthill [15], when he studied the generation of sound by a turbulent flow. More recently, the analysis was extended to water waves by exploiting the formal analogy between (non-dispersive) sound waves and waves in shallow water [4, 9]. Other approach, probably also influenced by Lighthill's work, was proposed by Phillips to study the interaction of a turbulent flow with surface water waves in an oceanographical setting [23].

Two important problems come from the interaction between turbulence and a restoring mechanism (as gravity) in the surface of a flow [4, 9, 23]: (a) the generation of waves; (b) the scattering of propagating waves. Both situations are presented in Fig. 1: left panel show a wavy surface which appears as a consequence of the underlying turbulent motion; right panel present a similar setup, where the surface is perturbed both by an underlying flow (although the forcing is almost ten times smaller compared to the left panel) and by a wave that is excited at the bottom-right corner. More details are given in Sects. 3.2 and 3.3, respectively.

In many situations it is important to measure the deformation of a liquid surface after a perturbation. From ripple tank experiments and its pedagogical interest of visualizing concepts of sound waves [14, 16, 29]; to more sophisticated experiments relating the statistical features of subsurface water motion with the one on the surface [25]. In the fifties, Cox and Munk pioneered the use of light to obtain spatially-resolved measurements of the deformation field of a fluid surface [6]. However, last years were prolific in the development of new measurement techniques to study water motion in the laboratory [2, 5, 21, 24, 31], taking advantage of different optical properties of water. Liquid metals, on the other hand, continue to be more elusive, since they are opaque and highly reflecting.

Liquid metals are relevant because they appear in planetary flows (see, for instance, [22]) and in industrial applications [7]. Among industrial problems, improvements in the efficiency of aluminum reduction cells largely depend on reliable measurements

and analysis of surface deformation. Here, the surface of liquid alumina (surmounted by lighter liquid electrolytes) exhibits instability as a consequence of a complex interaction between strong currents and magnetic fields. Control of the interfacial instability would allow to reduce the thickness of the electrolyte layer, considerably increasing the efficiency of the process [7].

This chapter organizes as follows. The measurement technique is described in Sect. 2. It consists on a classical geometrical arrangement to measure the profile of a surface, which is cleverly extended to a highly-reflecting liquid metal flow. We recall the optical arrangement first (Sect. 2.1). Then, it is discussed our particular setup and its practical advantages in the study of liquid metals (Sects. 2.2 and 2.3). Finally, we discuss the associated image processing (Sect. 2.4). Section 3 concerns the applications that motivated our study. We first describe the setup we use to study magnetohydrodynamical (MHD) flows (Sect. 3.1). Then we focus on the surface deformation induced by this flow (Sect. 3.2). Finally we give a brief account of what happens with a wave that propagates on the surface of the turbulent flow (Sect. 3.3). We end this chapter with the conclusions.

2 Measurement of Surface Deformation

The aim of this section is to present our method to perform surface level measurements along a line in a liquid metal.

2.1 Oblique View

The idea behind the method is very simple. It is conceptually the same as looking a surface profile with a camera perpendicular to it. This *perpendicular view* is particularly useful when the surface moves roughly on a single plane. Examples of this situation are quasi-unidimensional experiments, as those of solitary waves in water [10] or in granular layers [20]. The advantage of these methods is that one can directly obtain the surface profile, as naturally as in human vision.

However, we are interested in a surface which moves vertically in a large horizontal area. To do so, we perform observations on a single isolated line. This can be done, for instance, by illuminating the surface with a laser sheet from the top, and by looking to the light diffused on it, which is always moving jointly with the surface. In that case, the view of the line may be obstructed. It usually happen if part of the surface deforms strongly enough to cover the light path between the illuminated line and the observation point (at the camera position). To avoid obstructions, one can change the observation angle, going from a perpendicular view to an oblique one.

The geometry introduced for the oblique view is still very simple and it is shown in Fig. 2 for a single point (rather than for a line). We consider the paraxial approximation $\beta_{max} \approx H/L \ll 1$, as the distance L between the camera and the measurement area,

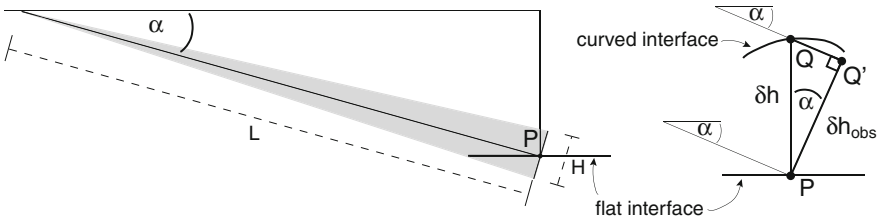

Fig. 2 Geometry linking the observed displacement δh_{obs} and the vertical displacement δh, in the paraxial approximation

is much larger than the maximal measured deformation H. In this approximation, one can consider a reference point P, lets say on the flat surface. Then, when the surface deforms, the point in the same vertical, Q will be perceived as being Q'. The vertical displacement $\overline{PQ} \equiv \delta h$ and the observed displacement $\overline{PQ'} \equiv \delta h_{obs}$ are related by

$$\delta h = \delta h_{obs} / \cos\alpha, \tag{1}$$

where α is the angle between the camera orientation direction and the horizontal (see Fig. 2). This argument is valid for a whole line. It is defined by the direction $\hat{r}$, and gives $\delta h(r) = \delta h_{obs}(r)/\cos\alpha$. The angle α lays between zero and $\pi/2$ (see (1) or Fig. 2). If α is close to zero, the measured δh_{obs} is very similar to the real δh, and the amplitude of motion can be directly obtained. However, in this case the view can be easily obstructed by other vertical deformations happening closer to the camera. For larger α on the other hand, obstructions are less probable, but to the detriment of the measured amplitude δh_{obs}. Despite δh is reconstructed geometrically, larger αs imply a lower resolution in the measurement. Therefore, α is chosen having in mind these two constrains.

2.2 Application to Highly Reflective Surfaces

A major challenge comes when using this technique in a highly reflecting surface, like the one of a liquid metal. This is because most of the light coming from the laser sheet is reflected specularly (i.e. in the vertical direction when the surface is flat). The consequence is twofold:

1. Only a small amount of light can be seen by diffusion (from any angle α). It is observed that the light diffusion properties are related to the cleanliness of the surface: the more impurities cumulate on the surface, the better the diffused line is seen. Therefore, the purest is the liquid metal, the more difficult will be to track the diffused line, although there is always possible to carry out the analysis in practical situations.
2. The reflected part of the beam coming to the surface (i.e. most of the light) is projected always specularly. As the surface deforms erratically, the reflected line

does as well. Eventually, the slope of the surface may be such that the reflected beam is in the observer direction, saturating the camera sensor. As expected, if the camera is placed with an angle α close to $\pi/2$, saturations occur frequently, even if the interfacial deformation is gentle. When α is reduced, saturations are less. Therefore, a third constrain is added to the choice of α.

2.3 Stereoscopic Extension

As it can be seen in Fig. 1, the flows under consideration have strong deformation. Thus, we expect to deal with saturations sooner or later. However, one can easily overcome the problem by putting a second camera on the opposite angle with respect to the vertical (they can be identified with M2 and M2′ in Fig. 3). If the surface is smooth, it has a well-defined slope at each point on the line. Therefore, if the reflection of a ray saturates a camera sensor, the same ray cannot saturate the sensor on the other camera at the same time.

Then, in the post-processing stage, one can reconstruct all the line by discarding the saturated parts of both simultaneous records. In practice, as the vertical deformation of the line could be registered within a few pixels, we decided to use a set of mirrors in order to register both views in a single picture (see Fig. 3). This trick has also the advantage of avoiding camera synchronization. As it is actually a stereoscopic measurement and it is performed with a single camera, we may call it *single camera stereoscopic measurement*.

A realization of the setup is schematized in Fig. 3. A laser sheet is obtained by placing a cylindrical lens *Le* in the path of a laser beam *La*. With the help of the mirror $M1$, the sheet is sent vertically to the liquid-metal surface, where part of the light diffuses along a line. The laser we use is a continuous green (wavelength of 532 nm). With an array of mirrors ($M2$, $M2'$ and P), images of the diffused line are

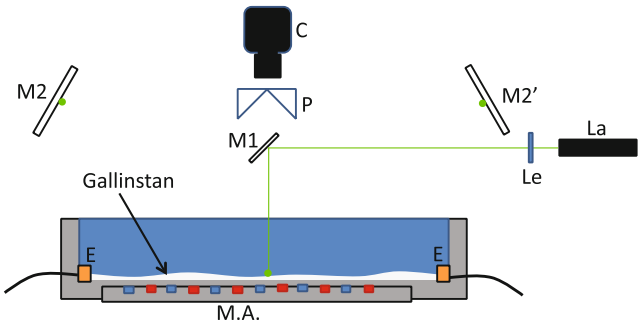

Fig. 3 Stereoscopic setup. A 1 cm layer of Gallinstan is placed between two electrodes (E), over a magnet array ($M.A.$) in a container of 50×40 cm^2. A laser La, a cylindrical lens Le and a mirror $M1$ produce a light sheet. The diffused line is tracked with two opposite angles by a single camera C, mirrors $M2$, $M2'$ and prisms P

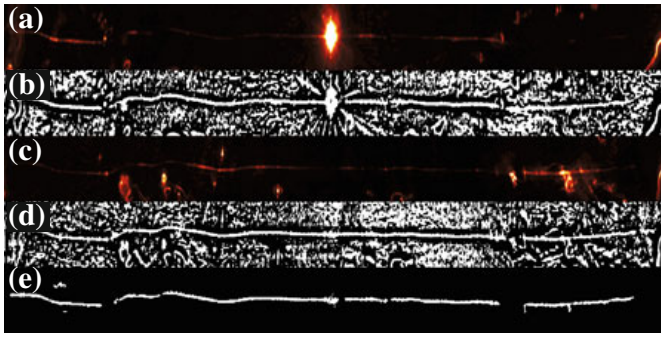

Fig. 4 Example of line reconstruction scheme. **a** and **c** are the two registered views. They are binarized in (**b**) and (**d**), respectively. The matrix multiplication is presented in (**e**) after noise removal. The flow under study is strong, produced with $I = 500$ A. A saturation is seen in (**a**)

sent to the camera C. The associated α angles are $\pm 50\,^{\circ}$. We take images at 60 Hz with a high resolution Dalsa camera that gives 2000×1700 pixels^2 images. When taking pictures of a line of 40 cm, one gets 5 pixels/mm as horizontal resolution. Vertical resolution depends on the angle α, and here it is found to be 3 pixels/mm. It was obtained by measuring the profile of a well calibrated stairway-shaped object.

2.4 Image Processing

Once images were obtained, the goal is to track the diffused line, converting it to a continuous and derivable function $\eta(x, t)$. The main steps for the analysis can be summarized as follows:

1. To remove any distortion between both views, induced by residual misalignments in the optical configuration. This can be achieved by performing a transformation (which may include translation, rotation and elongation) of one view. Once it is found for a single image-pair, it could be applied to the whole set of images. Further steps assume that both views are equivalent, with the only exception of saturated regions.
2. To filter the saturated spots. Here again we take advantage of the stereoscopic acquisition of images. It allows to filter one view with the complementary one. Among the several ways to do it, perhaps the simplest is to average the light intensity of both views. A slightly more complex procedure is shown in Fig. 4: each view is binarized and then both views are multiplied, eliminating saturated spots (see caption). After this step, we end up with a single image merging both views.
3. To extract a continuous line from the intensity map. Several methods are available, including very sophisticated global procedures [13, 32]. We computed the convolution with a Gaussian intensity profile for each line on the image.

Typical examples of the obtained deformation fields $\eta(x, t)$ are given in Sect. 3, in the form of spatiotemporal diagrams. These measurements also helped to characterize the flow obtained in our MHD setup [11].

3 Applications

Now we have a tool to study how a liquid-metal-surface is deformed. It can be either as a consequence of an underlying flow, or because of external perturbations. But before discussing our experimental results, we first present the setup used to produce the flow, together with its main characteristics.

3.1 Magnetohydrodynamical Setup

To stir a fluid in a constrained situation, we use a classical setup [3]. We apply the Lorentz force $\mathbf{F}_L = \mathbf{J} \times \mathbf{B}$, as depicted in Fig. 3. A vertical magnetic field $\mathbf{B}$ is produced with bands of strong permanent magnets with alternating polarities (named $M.A.$ in Fig. 3). The spatial structure of $\mathbf{B}$ fixes the one of the forcing. A horizontal density of current $\mathbf{J}$ is obtained by imposing an electrical current I between two electrodes placed on the container ends (named E in Fig. 3). The efficiency of this forcing depends on the fluid conductivity, justifying our choice of working with a liquid metal. We use Gallinstan, an alloy made of gallium, indium and tin, which is liquid at room temperature.[1] Thus, we can impose electrical currents I going from few Amperes to 600 with negligible heat losses. The control parameter of the experiment will be I. The characteristics of the flow were given elsewhere [11]. However, we can underline that the forcing is principally horizontal, and it has a fixed length scale. This produces several vortices of a size comparable with the one of the forcing (around 4 cm), which move and interact with each other, in a rather unpredictable way.

3.2 Deformation of the Surface of a Vortical Flow

We now focus on the surface deformation η produced by the underlying turbulent flow. An example of spatiotemporal evolution is shown in Fig. 5a, after the mean level is subtracted. Several features can be emphasized: (i) as expected for the motion of interacting vortices, surface deformation is highly fluctuating. (ii) The more visible deformation comes in large patches, and negative events (in blue) seem to have a characteristic width, despite it is not fixed. (iii) Negative events (*vortical depletions*) cover a smaller area in the diagram, although their magnitude is higher (the color-code is not symmetrical around zero). (iv) As a consequence of the conservation of mass, a larger area in the diagram has a level η larger than zero. (v) One can observe tenuous straight lines, specially in higher (red) zones.

[1] From the safety datasheet acc, Guideline 93/112/EC of Germatherm Medical AG, the Gallinstan is made of 68.5 % of Gallium, 21.5 % of indium, 10 % of Tin. Its density is $\rho = 6.440 \times 10^3$ kg/m^3, its kinematic viscosity is $\nu = 3.73 \times 10^{-7}$ m^2/s, its electrical conductivity $\sigma = 3.46 \times 10^6$ S/m.

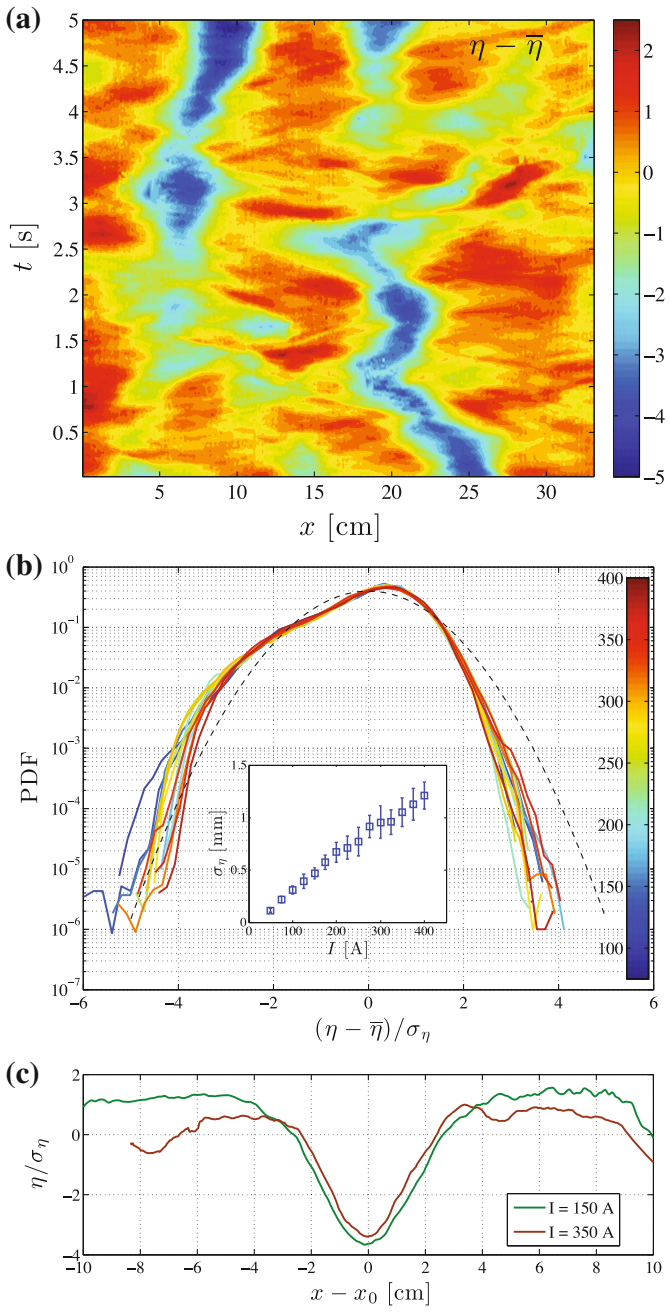

Fig. 5 Surface deformation induced by a vortex-dominated flow. Panel **a** present 5 s of the spatiotemporal evolution of η after the mean level $\overline{\eta}$ is subtracted. The MHD flow is produced here with an electrical current of $I =$ 350 A. Panel **b** present the PDF of $(\eta - \overline{\eta})/\sigma_\eta$, which is the deformation normalized by the standard deviation σ_η. The *color code* represent here the current I. The *black dashed line* correspond to a Gaussian distribution. The *inset* present σ_η as a function of I. Panel **c** show two examples of *vortex depletions*, where the hight η has been previously normalized. The position is given by x_0

From the whole measurement (of 60 s), we compute the statistics of the level η. The obtained probability distribution function (PDF) is shown in Fig. 5b for different intensities in the MHD forcing. Colors go from a gentle forcing in blue to a strong one in red. Remarkably, all these PDFs show a fair collapse when rescaled in terms of the standard deviation (shown as an inset in Fig. 5b), suggesting a common origin. However, they considerably differ from the Gaussian shape shown as a dashed

black line. The most probable value in the PDF is above zero, consistent with the observations made before.

Random linear waves—as those encountered in a calm ocean—show Gaussian PDFs [17, 26]. For gravity waves, when nonlinear effects become important, it appears an asymmetry between crests and troughs. It imposes an asymmetry in the PDF through positive values [18, 26, 30]. However, it was shown that the asymmetry can be removed by geometrical constrains for capillary waves, and Gaussian statistics are recovered [8]. The asymmetry of the PDFs is quantified with the skewness: it is zero for symmetric distributions (for instance for random linear waves) and positive for random nonlinear waves [27].

Our PDF, on the other hand, show an asymmetry through negative values. This is consistent with our previous observations of Fig. 5a, as we noticed that vortical depletions have an important contribution in η. Depletions are produced by a lower pressure at the vortex-core, and its magnitude depends on its vorticity, which in turbulence is expected to follow a Gaussian distribution. Thus, vortex profiles are intrinsically asymmetric through negative values with respect of the mean level of η (see two examples in Fig. 5c, where η has been normalized). This asymmetry is expected to impose the asymmetry in the distribution of η, expressed in a negative skewness. Note that, even if the PDF in Fig. 5b looks slightly similar to a bimodal distribution, we check that there is no second stable value for the surface level. Therefore, the PDF is shaped mainly by the statistical nature of vortical depletions.

A theoretical analysis inspired in this flow will be developed elsewhere. The idea is to consider the hydrodynamics of a single vortex without discharge (but inspired in those analysis [1, 19, 28]), combined with statistical arguments as in the study of random sea-waves.

We conclude that the main contribution to η comes from vortical structures interacting in a erratic way. However, as we noticed in Fig. 5a, one may also distinguish tenuous straight lines. As traveling waves appear as straight lines in spatiotemporal diagrams (see also Sect. 3.3), we may identify these features as the subtle signature of waves. The frequency spectrum of a velocity signal is less steep than the one of the position. Thus any wave-like motion present in our data should be emphasized by taking the temporal derivative. Indeed, in the example of $\partial\eta/\partial t$ shown in Fig. 6a, straight-line features appear much more clear than in the original signal.

From velocity signals, we computed the fast Fourier transform (FFT), which is shown in Fig. 6b. It presents a map of the frequencies and wavelengths involved in the motion. As the surface is perturbed from the bulk, the response in wavelength to a given frequency (the dispersion relation) is far from being known. Indeed, one can see that there is a large patch concentrating surface energy (from 0.2 to 3 Hz and from 0 to 0.25 cm^{-1}). As a reference, we plotted—in a thick white line—the usual dispersion relation for linear waves:

$$\omega^2 = \left(\frac{\rho-\rho'}{\rho+\rho'}gk + \frac{\gamma}{\rho+\rho'}k^3\right)\cdot\tanh(kH) \tag{2}$$

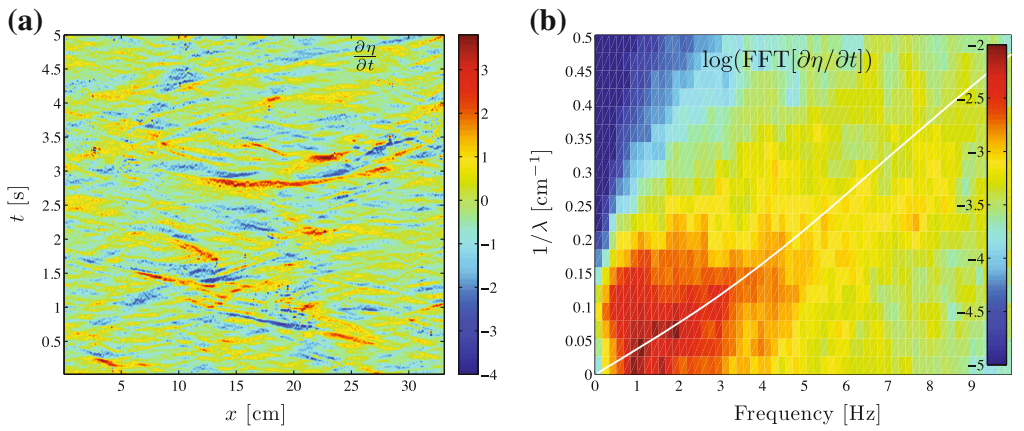

Fig. 6 Spatio-temporal diagram of the vertical velocity of the surface $\partial\eta/\partial t$ (*left*) and its fast Fourier transform (*right*) in log scale. The associated linear dispersion relation is added as a *thick white line* on the *right panel*. The forcing here corresponds to $I = 400$ A

where $k = 2\pi/\lambda$ is the wavenumber, λ is the wavelength, $\omega = 2\pi f$ is the angular frequency, H is the fluid depth, g is the gravity acceleration, γ is the surface tension, ρ is the liquid metal density and ρ' is the density of acidified-water used to prevent surface oxidation. We see that part of the surface energy lies on linear dispersion relation, despite it not confined to it at all. These result represent another experimental observation of waves generated by unstationary flows [5, 25]. However, a more proper identification of the structures containing surface energy is another perspective of this work.

3.3 Waves Propagating over a Turbulent Flow

We are interested now in what happens to a wave that propagates on the surface of the turbulent flow. The extensive study is described elsewhere [12]. Here we only explain our procedure, and we show typical deformations fields obtained with the measurement technique described before.

We excite waves on the liquid metal surface by means of an electromagnetic shaker. A vertical sinusoidal vibration is applied to the liquid surface by a cylindrical paddle. This *source* of waves is placed on one corner of the working area (bottom-right corner in Fig. 1 and near the x-origin in Fig. 7), and measurements are performed along the central line in the container. Figure 7 present our typical observations. In Fig. 7a, there is only the mechanically excited wave (here at $f_0 = 5$ Hz). Wave propagation appears very clear as oblique lines, despite the wave pattern is not completely trivial. Figure 7b present the deformation of the surface when there are both a wave (again at $f_0 = 5$ Hz) and an underling fluid motion produced by MHD forcing at $I = 80$ A. In this case, the contributions to surface deformation are easy to identify: waves correspond to oblique lines (as in left panel), and the big red and blue

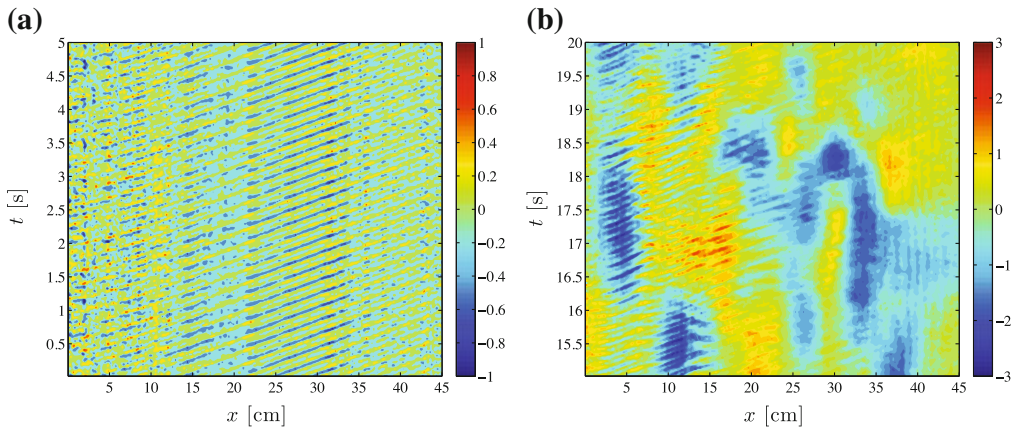

Fig. 7 Spatio-temporal diagrams of the surface displacement η. They show the influence of fluid motion on the propagation of waves. *Left* a wave is excited externally at 5 Hz with a shaker. *Right* the same wave is propagating over a fluctuating background produced by a forcing of $I = 80$ A

patches correspond to larger scale fluid motion. Interestingly, one may appreciate here that the amplitude of the propagating wave gradually decreases. It is visible only until around $x \sim 25$ or 30 cm, as a consequence of an enhanced dissipation produced by fluid motion.

To go further in the study, we measure η for different flow strengths (controlled by the current I) and for excitation frequencies f_0 between 3 and 9 Hz. Knowing that I and the flow velocity U_o are related as $U_o \sim \sqrt{I}$ [11], we can define the Froude number $Fr = U_o/C_w$, where C_w is the phase velocity of the wave. Two main results come from our observations: (a) Wave dissipation is enhanced by the flow, as observed in Fig. 7b. This enhanced dissipation is found to scale linearly with Fr. (b) A shift in the wavelength is found for frequencies between 6 and 9 Hz. The shift can also be described as a function of Fr. A detailed account of these results is given in [12].

4 Conclusions

In this chapter we present a conceptually simple technique to perform measurements of the surface deformation in the highly-reflecting surface of a liquid metal. The idea is to send a laser sheet on the surface of the liquid-metal and to track the diffused light with a camera from a given angle. When the deformation of the surface is strong, specular reflections of the laser saturates the camera sensor. This problem is overcome by using an optical arrangement allowing to record two complementary views of the diffused line in the same picture.

The technique is used to study two problems of the interaction between surface waves and turbulent flows. First we considered the influence of turbulence on surface deformation. The statistics of the height level are presented. They are asymmetric,

with a negative asymmetry coefficient (skewness), in opposition to steep gravity waves, were the skewness is positive. This is interpreted as a statistical signature of vortices. Then, we discussed the presence of wavy motion in our signals, highlighted in the vertical velocity of the surface.

Finally, we present some observations about the influence of turbulence on wave propagation. Here we considered simultaneously our turbulent MHD flow and externally excited waves. Wave dissipation by turbulence is visible in a presented spatiotemporal diagram. A more complete study is given elsewhere [12].

Acknowledgments We would like to thanks C. Wiertel-Gasquet for helping with the automation of the experiment. F. Daviaud, M. Bonetti and G. Zalczer for helpful discussions. PG received support from the Triangle de la Physique and CONICYT/FONDECYT postdoctorado N 3140550.

References

1. A. Andersen, T. Bohr, B. Stenum, J. Juul Rasmussen, B. Lautrup, The bathtub vortex in a rotating container. J. Fluid Mech. **556**, 121–146 (2006)
2. A. Benetazzo, Measurements of short water waves using stereo matched image sequences. Coast. Eng. **53**, 1013–1032 (2006)
3. N.F. Bondarenko, M.Z. Gak, F.V. Dolzhanskiy, Laboratory and theoretical models of plane periodic flow. Izv. Atmos. Ocean. Phys. **15**, 711–716 (1979)
4. E. Cerda, F. Lund, Interaction of surface waves with vorticity in shallow water. Phys. Rev. Lett. **70**, 3896–3899 (1993)
5. P.J. Cobelli, A. Maurel, V. Pagneux, P. Petitjeans, Global measurement of water waves by Fourier transform profilometry. Exp. Fluids **46**, 1037–1047 (2009)
6. C. Cox, W. Munk, Measurement of the roughness of the sea surface from photographs of the sun's glitter. J. Opt. Soc. Am. **44**, 838–850 (1954)
7. P.A. Davidson, Magnetohydrodynamics in materials processing. Annu. Rev. Fluid Mech. **31**, 273–300 (1999)
8. G. Düring, C. Falcón, Symmetry induced four-wave capillary wave turbulence. Phys. Rev. Lett. **103**, 174503 (2009)
9. R. Ford, Gravity wave generation by vortical flows in a rotating frame. Ph.D. thesis, University of Cambridge, 1993
10. L. Gordillo, T. Sauma, Y. Zárate, I. Espinoza, M.G. Clerc, N. Mujica, Can non-propagating hydrodynamic solitons be forced to move? Eur. Phys. J. D **62**, 39–49 (2010)
11. P. Gutiérrez, S. Aumaître, Clustering of floaters on the free surface of a turbulent flow: an experimental study. (2015)
12. P. Gutiérrez, S. Aumaître, Surface waves propagation on a turbulent flow forced electromagnetically (2015)
13. M. Kass, A. Witkin, D. Terzopoulos, Snakes: active contour models. Int. J. Comput. Vis. **1**, 321–331 (1988)
14. G. Kuwabara, T. Hasegawa, K. Kono, Water waves in a ripple tank. Am. J. Phys. **54**, 1002–1007 (1986)
15. M.J. Lighthill, On sound generated aerodynamically. I. General theory. Proc. R. Soc. Lond. A 211, 564–587 (1952)
16. M.J. Lighthill, Waves in Fluids (Cambridge University Press, Cambridge, 1978)
17. M.S. Longuet-Higgins, The statistical analysis of a random, moving surface. Phil. Trans. R. Soc. Lond. A **249**, 321–387 (1957)
18. M.S. Longuet-Higgins, On the distribution of the heights of sea waves: some effects of nonlinearity and finite band width. J. Geophys. Res. **85**, 1519–1523 (1980)

19. T.S. Lundgren, The vortical flow above the drain-hole in a rotating vessel. J. Fluid Mech. **155**, 381–412 (1985)
20. J.E. Macías, C. Falcón, Dynamics of spatially modulated kinks in shallow granular layers. New J. Phys. **16**, 043032 (2014)
21. F. Moisy, M. Rabaud, K. Salsac, A synthetic Schlieren method for the measurement of the topography of a liquid interface. Exp. Fluids **46**, 1021–1036 (2009)
22. R. Monchaux, M. Berhanu, M. Bourgoin, M. Moulin, P. Odier, J.F. Pinton, R. Volk, S. Fauve, N. Mordant, F. Pétrélis, A. Chiffaudel, F. Daviaud, B. Dubrulle, C. Gasquet, L. Marie, F. Ravelet, Generation of a magnetic field by dynamo action in a turbulent flow of liquid sodium. Phys. Rev. Lett. **98**, 044502 (2007)
23. O.M. Phillips, The scattering of gravity waves by turbulence. J. Fluid Mech. **5**, 177–192 (1959)
24. R. Savelsberg, A. Holten, W. van de Water, Measurement of the gradient field of a turbulent free surface. Exp. Fluids **41**, 629–640 (2006)
25. R. Savelsberg, W. van de Water, Turbulence of a free surface. Phys. Rev. Lett. **100**, 034501 (2008)
26. H. Socquet-Juglard, K. Dysthe, K. Trulsen, H.E. Krogstad, J. Liu, Probability distributions of surface gravity waves during spectral changes. J. Fluid Mech. **542**, 195–216 (2005)
27. M.A. Srokosz, M.S. Longuet-Higgins, On the skewness of sea-surface elevation. J. Fluid Mech. **164**, 487–497 (1986)
28. Y. Stepanyants, G. Yeoh, Stationary bathtub vortices and a critical regime of liquid discharge. J. Fluid Mech. **604**, 77–98 (2008)
29. B. Ströbel, Demonstration and study of the dispersion of water waves with a computer-controlled ripple tank. Am. J. Phys. **79**, 581–589 (2011)
30. M.A. Tayfun, Narrow-band nonlinear sea waves. J. Geophys. Res. **85**, 1548–1552 (1980)
31. W.B. Wright, R. Budakian, S.J. Putterman, Diffusing light photography of fully developed isotropic ripple turbulence. Phys. Rev. Lett. **76**, 4528–4531 (1996)
32. C. Xu, J.L. Prince, Snakes, shapes, and gradient vector flow. IEEE Trans. Image Process. **7**, 359–369 (1998)